International Journal of Heat and Mass Transfer 54 (2011) 5087–5099

Contents lists available at ScienceDirect

International Journal of Heat and Mass Transfer

journal homepage: www.elsevier.com/locate/ijhmt

Combined heat transfer of radiation and natural convection in a square cavity containing participating gases

K. Lari [a], M. Baneshi [b], S.A. Gandjalikhan Nassab [a], A. Komiya [b], S. Maruyama [b,*]

[a] Department of Mechanical Engineering, School of Engineering, Shahid Bahonar University, Kerman, Iran
[b] Institute of Fluid Science, Tohoku University, 2-1-1 Katahira, Aoba-ku, Sendai 980-8577, Japan

ARTICLE INFO

Article history:
Received 8 December 2010
Received in revised form 8 June 2011
Accepted 6 July 2011
Available online 5 August 2011

Keywords:
Radiation
Natural convection
Square cavity
Normal room conditions
Discrete ordinates method

ABSTRACT

This article deals with analyzing the effect of radiative heat transfer on natural convection heat transfer in a square cavity under normal room conditions. The governing equations of natural convection and radiative transfer are solved simultaneously to obtain the temperature, velocity and heat flux distributions inside the participating medium. The finite volume method has been adopted to solve the governing equations and the discrete ordinates method (DOM) is used to model the radiative transfer in absorbing-emitting media. The radiative–convective model is validated by comparison with test cases solutions from the literature. Then, the effects of Rayleigh number from 10^2 to 10^6 and optical thickness in a broad range from 0 to 100 on temperature and velocity distributions and Nusselt numbers are investigated. The results show that even under normal room conditions with a low temperature difference, the radiation plays a significant role on temperature distribution and flow pattern in the cavity. Also, several interesting effects of radiation are observed such as a sweep behavior on the isotherms, streamlines and velocity distributions of the cavity along the optical thickness and a reverse behavior on maximum stream function and convective Nusselt number at different Rayleigh numbers.

1. Introduction

Natural convection is important in many areas such as in double-glazed windows, solar collectors, cooling devices for electronic instruments and building insulations. In the literature, a lot of works have been done over the last four decades in the area of numerical and experimental natural convection.

Among the past works, de Vahl Davis [1] did a numerical calculation to obtain results for a square cavity at Rayleigh numbers (Ra) between 10^3 and 10^6 as a benchmark solution. Churchill [2] in his work suggested some empirical formulation and graphs to calculate the Nusselt number (Nu) at different Rayleigh numbers and cases based on many theoretical and experimental results. Markatos and Pericleous [3] studied natural convection in the square cavity for both laminar and turbulence flow. Three-dimensional steady-state natural convection of air was investigated by Fusegi et al. [4]. Their graphs revealed the three-dimensional behavior of the laminar flow. Also, Barakos et al. [5] studied the laminar and turbulence flow in the square cavity and compared their works with experimental data and previous numerical results.

Pesso and Piva [6] presented a numerical study of steady natural convection at low Prandtl numbers caused by large density differences. The effects of the Rayleigh, Prandtl and Gay-Lussac numbers on the Nusselt number at the walls of the square cavity were investigated in their work and a heat transfer correlation was proposed. Heat transfer enhancement in the square cavity was analyzed by Jahanshahi et al. [7] using the water/SiO_2 nanofluid. They used an experimental setup to calculate the conductivity value of nanofluid. Maruyama et al. investigated natural convection in cavities [8], ducts [9–11] and pin fins [12].

Radiative heat transfer plays an important role in heat transfer in cavities. In the coupled radiation and natural convection, many works take only into account the effects of surface-to-surface radiation in order to reduce computational effort [13–17]. The effect of participating gasses, such as CO_2 and water vapor which emit and absorb thermal radiation, is important in heat transfer in cavities. Radiation of participating gasses cannot be neglected even at a normal temperature range. For example, radiation emitted by a wall at 300 K is absorbed by 30% during the path length of 10 m [18]. These participating gasses sometimes treated as gray gasses whose radiative properties are independent of the wavelengths.

Among the works with assumption of gray media, Tan and Howell [19] studied the benchmark problem of square cavity with the exact integral formulation for solving the radiative transfer equation. They concluded that the presence of radiation will increase the bulk temperatures of the fluid, and may have a significant influence on the fluid flow and temperature distributions. The effects of radiation on steady-laminar natural convection in a rectangular enclosure with two incomplete partitions are numerically

* Corresponding author.
E-mail address: maruyama@ifs.tohoku.ac.jp (S. Maruyama).

0017-9310/$ - see front matter © 2011 Elsevier Ltd. All rights reserved.
doi:10.1016/j.ijheatmasstransfer.2011.07.026

Nomenclature

c_p	specific heat capacity (J/kg K)
g	gravitational acceleration (m/s^2)
I	radiation intensity (W/m^2 sr)
$\bar{I}$	dimensionless radiation intensity
K	thermal conductivity (W/m K)
L	length (m)
M	number of discrete directions
N	unit vector normal to the surface
Nu	Nusselt number
$\overline{Nu}$	average Nusselt number
P	pressure (Pa)
Pl	Planck number
Pr	Prandtl number
q	heat flux (W/m^2)
$\dot{q}'''$	heat generation per unit volume (W/m^3)
Q	dimensionless heat flux
r	position vector
Ra	Rayleigh number
S	source term (W/m^3)
t	time (s)
T	temperature (K)
T_{ave}	average temperature = $(T_h + T_c)/2$
ΔT	temperature difference = $T_h - T_c$
u, v	x- and y-component of velocity (m/s)
U, V	dimensionless x- and y-component of velocity
W	weight of angular quadrature
x, y, z	coordinate (m)
X, Y, Z	dimensionless coordinate

Greek symbols

α	thermal diffusivity (m^2/s)
β	extinction coefficient (m^{-1}), or coefficient of thermal expansion (K^{-1})
ε	emissivity of a surface
θ	dimensionless temperature
θ_{ave}	dimensionless average temperature
κ	absorption coefficient (m^{-1})
ξ, η, μ	x-, y- and z-direction cosines
ρ	density (kg/m^3)
σ	Stefan–Boltzmann constant = 5.670×10^{-8} W/m^2 K^4
σ_s	scattering coefficient (m^{-1})
τ	optical thickness
υ	kinematic viscosity (m^2/s)
ϕ	general parameter (defined when used)
Φ	scattering phase function
Ψ	stream function (m^2/s)
Ψ	dimensionless stream function
ω	scattering albedo
Ω	direction vector

Subscripts

b	black body
c	convective term, or cold wall
h	hot wall
k	index of sigma
m	discrete direction
ove	overall
p	nodal point
r	radiative term
w	wall
x, y, z	coordinate

Superscripts

*	dimensionless
$'$	incoming direction
m	discrete direction
n	iteration step

examined in the work of Han and Baek [20]. They used the finite volume method (FVM) to solve the radiative transfer equation (RTE) and showed that the surface radiation played a more important role than the gas radiation. Mondal and Mishra [21] used the lattice Boltzmann method (LBM) for the analysis of natural convection in the presence of volumetric radiation in a square cavity and FVM for solving RTE. They investigated the effects of different parameters such as Rayleigh number, convection–radiation parameter, extinction coefficient, and scattering albedo. They showed that for a high value of the Ra, the velocity field is significantly affected by radiation.

Recently, combined radiation and natural convection in a three-dimensional differentially heated rectangular cavity was analyzed by Kumar and Eswaran [22]. They used a non-Boussinesq variable density approach to incorporate density changes and finite volume method to solve the governing equations. They obtained results for just one Rayleigh number ($Ra = 10^5$) and the range of optical thicknesses from 0 to 100. Their results showed a complex flow field. They found that the temperature field is two-dimensional but the velocity field is three-dimensional.

Due to the difficulty in finding the exact analytical solution to integro-differential radiative transfer equation (RTE) in participating media, a variety of numerical methods have been worked out over the last few decades. They include the zone method, Monte Carlo method, flux method, discrete transfer method, P_N method, discrete ordinates method (DOM), finite volume method, REM^2, etc. Each of these methods has its own relative advantages and disadvantages, and none of them is superior to others in all aspects. In this respect, there exist two competing methods that share many researchers' interest: the discrete transfer method (DTM) and the discrete ordinates method (DOM), and their variations and improvements [23]. The method of discrete ordinates DOM is an attractive simplified method to solve radiative transfer problems. It offers a good compromise between accuracy and computational requirements. In particular, the DOM was originally formulated by Chandrasekar in 1950 [24], and has been deeply studied by Carlson and Lathrop in 60–70s [25] and by Fiveland and Truelove in the 80s [26,27]. Mishra et al. [28] suggested a new quadrature scheme for the DOM in which evaluation of ordinates and their corresponding weights is very simple.

In studies focused on natural convection, the radiative mode of heat transfer is sometimes neglected because of the overwhelming amount of computational resources it requires. Some literatures try to show that radiation heat transfer has an important and significant effect on the system and cannot be neglected [19,20]. However, some of previous described literatures used the unrealistic conditions for the square cavity (by using only non-dimensional properties) and/or high temperature difference to show the effect of radiation on the cavity. Besides, because of difficulties in obtaining accurate experimental data with small convective heat flux compared with radiative heat flux, experimental data of natural convection in enclosures are generally less accurate than for forced convection [2]. Therefore, accurate numerical computations in combined heat transfer can be valuable.

Hence, the objective of this work is investigating the effect of radiation on natural convection heat transfer in a square cavity

under normal room conditions (with low temperature difference) by using a precise numerical analysis with a broad range of Rayleigh numbers ($10^2 \leqslant Ra \leqslant 10^6$) and optical thicknesses ($0 \leqslant \tau \leqslant 100$). To achieve this goal, in the present study, a false-transient numerical procedure is offered to model the mentioned problem. The cavity is considered as an absorbing-emitting media with gray gases and the radiative transfer equation is solved using the conventional DOM. The finite volume method [29,30] has been adopted to solve the other governing equations and the radiative source term in the energy equation is computed from intensities field. The radiative convective model is validated by comparison with the well-documented results in literature. This model is applied to determine the temperature, velocity and stream function distributions of the domain at large varieties of Rayleigh numbers and optical thicknesses. Also, the effect of these parameters on the Nusselt numbers at the walls is thoroughly investigated.

2. Mathematical model

The geometry of the problem as shown in Fig. 1 is a square cavity by two horizontal insulating walls, and two vertical isothermal walls at different temperatures, T_h and T_c ($T_h > T_c$), respectively. All the physical properties in the system are assumed to be constant, except for the density. The participating medium is assumed to be gray, and the emissivities of the walls are also assumed to be constant.

2.1. Governing equations

The governing conservation equations for a two-dimensional, unsteady, laminar and constant property flow assuming Boussinesq approximation to be valid are:

$$\text{Continuity}: \quad \frac{\partial u}{\partial x}+\frac{\partial v}{\partial y}=0, \tag{1}$$

$$x\text{-momentum}: \quad \frac{\partial u}{\partial t}+u\frac{\partial u}{\partial x}+v\frac{\partial u}{\partial y}=-\frac{1}{\rho}\frac{\partial p}{\partial x}+\upsilon\left(\frac{\partial^2 u}{\partial x^2}+\frac{\partial^2 u}{\partial y^2}\right), \tag{2}$$

$$y\text{-momentum}: \quad \frac{\partial v}{\partial t}+u\frac{\partial v}{\partial x}+v\frac{\partial v}{\partial y}=-\frac{1}{\rho}\frac{\partial p}{\partial y}+\upsilon\left(\frac{\partial^2 v}{\partial x^2}+\frac{\partial^2 v}{\partial y^2}\right)+\beta g(T-T_{ave}), \tag{3}$$

$$\text{Energy}: \quad \frac{\partial T}{\partial t}+u\frac{\partial T}{\partial x}+v\frac{\partial T}{\partial y}=\alpha\left(\frac{\partial^2 T}{\partial x^2}+\frac{\partial^2 T}{\partial y^2}\right)-\frac{1}{\rho c_p}\nabla.q_r. \tag{4}$$

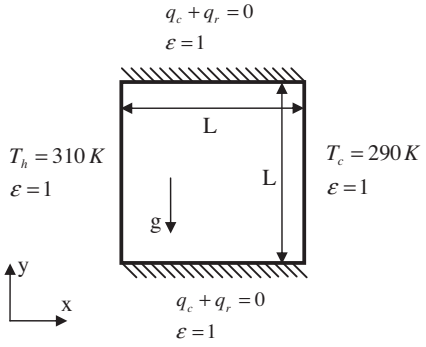

Fig. 1. The geometry of the cavity.

The local divergence of the radiative flux $\nabla.q_r$ in the energy equation (Eq. (4)) is related to the local intensities by:

$$\nabla.q_r=\kappa\left(4\pi I_b(r)-\int_{4\pi} I(r,\Omega)\,d\Omega\right). \tag{5}$$

To obtain the radiation intensity field and $\nabla.q_r$, it is necessary to solve the radiative transfer equation (RTE). This equation for an absorbing, emitting and scattering gray medium can be written as [31]:

$$(\Omega.\nabla)I(r,\Omega)=-\beta I(r,\Omega)+\kappa I_b(r)+\frac{\sigma_s}{4\pi}\int_{4\pi} I(r,\Omega')\Phi(\Omega,\Omega')\,d\Omega'. \tag{6}$$

It is noted that the RTE has to be solved in a three dimensional domain whereas the flow field is solved in two dimensional coordinates.

For equations (1)–(4), the initial conditions are $u = v = 0$, $p = 0$ and $T = T_{ave}$. For the velocity field the no-slip boundary condition is assumed. For the energy equation, the left wall is at T_h, the right wall is at T_c and the horizontal walls have the adiabatic condition ($q_c + q_r = 0$). The radiative heat flux on the boundary surfaces (q_r) can be expressed as:

$$q_r=\varepsilon\left(\pi I_b(r_w)-\int_{n.\Omega'<0} I(r_w,\Omega')|n.\Omega'|\,d\Omega'\right). \tag{7}$$

And the radiative boundary condition for diffusely reflecting surfaces in Eq. (6) is:

$$I(r_w,\Omega)=\varepsilon I_b(r_w)+\frac{(1-\varepsilon)}{\pi}\int_{n.\Omega'<0} I(r_w,\Omega')|n.\Omega'|\,d\Omega'. \tag{8}$$

2.2. Radiative transport equation

In this work the equation of radiation transport (Eq. (6)) is solved using the discrete ordinates method (DOM). In this method, the RTE is substituted by a set of M discrete equations for a finite number of directions Ω_m, and each integral is substituted by a quadrature series of the form:

$$(\Omega_m.\nabla)I(r,\Omega_m)=-\beta I(r,\Omega_m)+\kappa I_b(r)+\frac{\sigma_s}{4\pi}\sum_{k=1}^{M} w_k I(r,\Omega_k)\Phi(\Omega_m,\Omega_k) \tag{9}$$

subject to the boundary condition:

$$I(r_w,\Omega_m)=\varepsilon I_b(r_w)+\frac{(1-\varepsilon)}{\pi}\sum_{n.\Omega_k<0} w_k I(r_w,\Omega_k)|n.\Omega_k|, \tag{10}$$

where w_k is the ordinate weight. This angular approximation transforms the original equation into a set of coupled differential equations. In Cartesian coordinates, Eq. (9) becomes:

$$\xi_m\frac{\partial I_m}{\partial x}+\eta_m\frac{\partial I_m}{\partial y}+\mu_m\frac{\partial I_m}{\partial z}+\beta I_m=\beta S_m, \tag{11}$$

$$S_m=(1-\omega)I_b(r)+\frac{\omega}{4\pi}\sum_{k=1}^{M} w_k I(r,\Omega_k)\Phi(\Omega_m,\Omega_k), \tag{12}$$

where ξ_m, η_m and μ_m are the directional cosines of Ω_m, S_m represents the source term and $\omega = (\sigma_s/\beta)$ is scattering albedo.

The reflection boundary condition in Cartesian coordinates should be imposed in an appropriate manner. For example, for a surface parallel to the y–z-plane, with $n.\Omega_k = \xi_k$, we have for all k with $\xi_k > 0$ ($M/2$ boundary conditions):

$$I_m=\varepsilon I_b+\frac{(1-\varepsilon)}{\pi}\sum_{\substack{k\\ \xi_k<0}} w_k|\xi_k|I_k. \tag{13}$$

2.3. Dimensionless parameters

The non-dimensional form of Eqs. (1)–(6) can be obtained by using these dimensionless variables:

$$U = uL/\alpha, \quad V = vL/\alpha, \quad X = x/L, \quad Y = y/L, \quad t^* = t\alpha/L^2,$$
$$\theta = (T - T_c)/\Delta TP = pL^2/\rho\alpha^2, \quad \bar{I} = I/\sigma T_c^4, \quad S = s/L, \quad Q = q/\sigma T_c^4,$$
$$\Psi = \psi/\alpha Pr = \upsilon/\alpha, \quad Ra = \beta g \Delta T L^3/\upsilon\alpha, \quad Pl = \frac{k}{L\sigma T_c^3}, \quad \phi = \Delta T/T_c. \tag{14}$$

$$\text{Continuity}: \quad \frac{\partial U}{\partial X} + \frac{\partial V}{\partial Y} = 0, \tag{15}$$

$$x\text{-momentum}: \quad \frac{\partial U}{\partial t^*} + U\frac{\partial U}{\partial X} + V\frac{\partial U}{\partial Y} = -\frac{\partial P}{\partial X} + Pr\left(\frac{\partial^2 U}{\partial X^2} + \frac{\partial^2 U}{\partial Y^2}\right), \tag{16}$$

$$y\text{-momentum}: \quad \frac{\partial V}{\partial t^*} + U\frac{\partial V}{\partial X} + V\frac{\partial V}{\partial Y} = -\frac{\partial P}{\partial Y} + Pr\left(\frac{\partial^2 V}{\partial X^2} + \frac{\partial^2 V}{\partial Y^2}\right) + Ra\,Pr(\theta - \theta_{ave}), \tag{17}$$

$$\text{Energy}: \quad \frac{\partial \theta}{\partial t^*} + U\frac{\partial \theta}{\partial X} + V\frac{\partial \theta}{\partial Y} = \left(\frac{\partial^2 \theta}{\partial X^2} + \frac{\partial^2 \theta}{\partial Y^2}\right) - \frac{1}{Pl\phi}\nabla^*.Q_r, \tag{18}$$

$$\text{Divergence of the radiative flux}: \quad \nabla^*.Q = \tau(1-\omega)\left(4(\theta\phi + 1)^4 - \int_{4\pi} \bar{I} d\Omega\right) \tag{19}$$

$$\text{RTE}: \quad \frac{1}{\tau}(\Omega.\nabla^*)\bar{I} = \frac{(1-\omega)}{\pi}(\theta\phi + 1)^4 - \bar{I} + \frac{\omega}{4\pi}\int_{4\pi} \bar{I}\Phi d\Omega'. \tag{20}$$

The convective, radiative and overall Nusselt number at the walls are calculated from the heat fluxes as:

$$\text{Convective Nusselt Number}: \quad Nu_c = \frac{q_c L}{k\Delta T}, \tag{21}$$

$$\text{Radiative Nusselt Number}: \quad Nu_r = \frac{q_r L}{k\Delta T}, \tag{22}$$

$$\text{Overall Nusselt Number}: \quad Nu_{ove} = Nu_c + Nu_r. \tag{23}$$

The average Nusselt number $\overline{Nu}$ at the wall is the line-averaged value of Nu.

3. Numerical method

The strategy used to solve the Navier–Stokes and energy equations (Eqs. (16)–(18)) is a false-transient technique. The discretization of these equations is carried out using explicit finite volume techniques on Cartesian staggered grids [29,30]. To account for the velocity–pressure coupling, the HSMAC algorithm is adopted [32]. The QUICK scheme is used for convective terms. The mesh is refined near the walls to accurately capture the temperature and velocities variations in the boundary layer. Fig. 2 shows the refined mesh for 41×41 (Fig. 2(a)) and 81×81 (Fig. 2(b)) grid numbers.

The radiation source term in energy equation is calculated by solving RTE using DOM method. In order to consider all of the radiation effects in the problem, the RTE is solved in three-dimensional coordinates. For this purpose, the domain in Fig. 1 has been extended enough in z direction to have two-dimensional condition for natural convection. The finite volume technique is used to discretize the spatial part of the RTE and an iterative procedure is employed to determine the intensity radiation field. The discretization details and solution procedure can be found in [31]. The employed angular quadrature set is the S_N

1. The solution technique is briefly stated as follows:
2. Initialize the velocity, temperature, and intensity field.
3. Solve the RTE with the current temperature field until convergence.
4. Compute the divergence radiative source term using equation (19).
5. Solve the coupled velocity and temperature field, for one time step, with the above radiative source term.
6. Update the temperature field.
7. Repeat 2–5 for successive time steps until the velocity and temperature fields achieve steady state conditions.

The convergence criterion for the RTE and the steady state criteria for other governing equations are as follows, respectively:

$$Max\left|\frac{\bar{I}_p^n - \bar{I}_p^{n-1}}{\bar{I}_p^n}\right| \leqslant 10^{-6}, \tag{24}$$

$$Max\left|\frac{\phi_p^n - \phi_p^{n-1}}{\phi_p^n}\right| \leqslant 10^{-6}, \tag{25}$$

where ϕ can be U, V and θ.

4. Code and results verifications

For verification of the numerical solutions several validations have been done in this work.

4.1. Pure convection validation

In order to validate the convection part of the program, the problem described in Fig. 1 has been solved without radiation. In Table 1, the average Nusselt number at the hot wall for different Rayleigh numbers is shown and compared with previous results in the literature. The numbers in the parenthesis show the number of grids used in each side of the cavity to obtain each result.

To obtain accurate results, precise computation has been done. For each value of Ra the number of grids has been increased progressively until variation in the average Nusselt number becomes very small. This variation for different Ra can be observed in Fig. 3. In this figure, in order to plot the average Nusselt number at different Ra in one graph, the normalized average Nusselt number (the ratio of average Nusselt number in each grid number to the last one) is used. Then this normalized average Nusselt number is plotted versus grid numbers.

4.2. DOM validation

To check the validity of the discrete ordinates method, a test problem is considered with a cubic domain. This test is done on a furnace enclosure previously analyzed by Sakami et al. [33] by use of a new algorithm based on the discrete ordinates method and with the exponential spatial discretization scheme. The geometry is a parallelepiped with $L_x = L_y = 2$ m and $L_z = 4$ m. The gases inside the furnace are assigned to have a $\dot{q}''' = 5$ kW/m^3 volumetric heat source and an absorption coefficient $\kappa = 0.5$ m^{-1}. In this case, the RTE is coupled with the energy equation as follows:

$$\nabla q_r = \dot{q}'''. \tag{26}$$

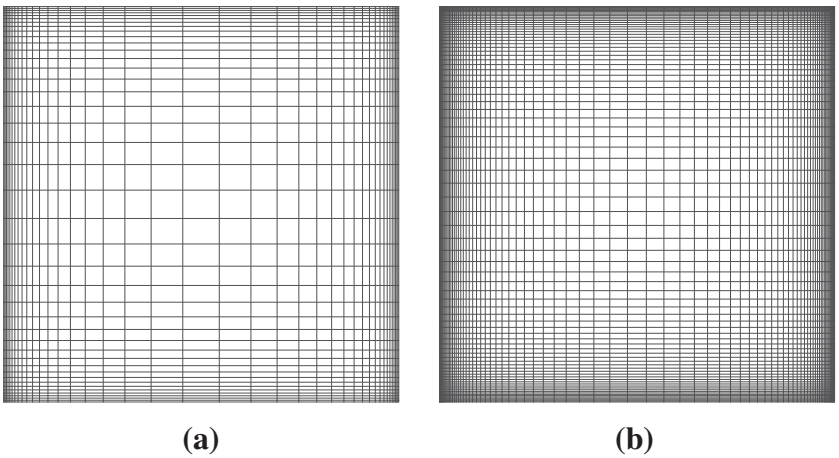

Fig. 2. The refined mesh for (a) 41 × 41 and (b) 81 × 81 grid numbers.

Table 1
Average Nusselt number at different *Ra*.

$\overline{Nu}_h$	Current work	Barakos et al. [5]	Fusegi et al. [4]	Markatos and Pericleous [3]	de Vahl Davis[1]	Churchill [2]
$Ra = 10^3$	1.122 (161)	1.114	1.134	1.108	1.118	1.05
$Ra = 10^4$	2.244 (161)	2.245	2.274	2.201	2.243	2.77
$Ra = 10^5$	4.518 (201)	4.510	4.568	4.430	4.519	4.95
$Ra = 10^6$	8.814 (421)	8.806	8.935	8.754	8.799	8.82

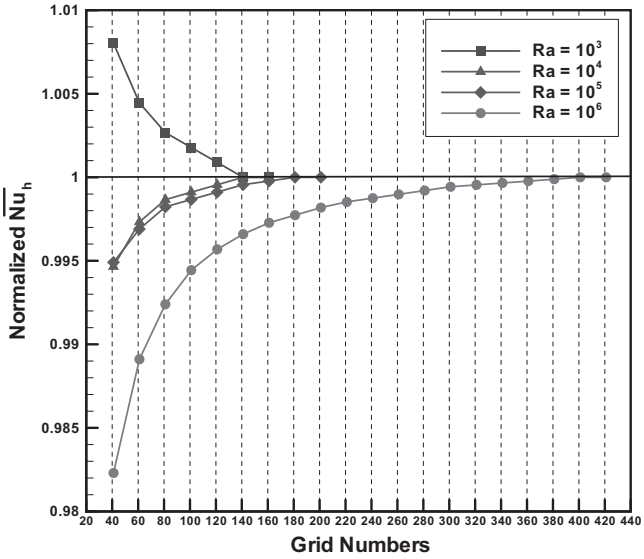

Fig. 3. Normalized average Nusselt number vs. grid numbers for different *Ra*.

The following boundary conditions are used:

at $z = 0$, $T = 1200$ K and $\varepsilon = 0.85$
at $z = L_z$, $T = 400$ K and $\varepsilon = 0.70$
and at the other surfaces, $T = 900$ K and $\varepsilon = 0.70$.

The solution is obtained using $8 \times 8 \times 12$ control volumes. The S_4 predicted gas temperature distributions at $y = 1$ m at different z-locations are shown in Fig. 4. They are compared with those obtained by the DOM method of Sakami's [33] work and by the zone method [33]. Good agreement is seen in this figure between results of the present work and the other results in the literature.

Fig. 5 shows the predicted radiative heat flux at the cold and hot walls. It can still be observed that the results obtained in the present work are in good agreement with previous studies.

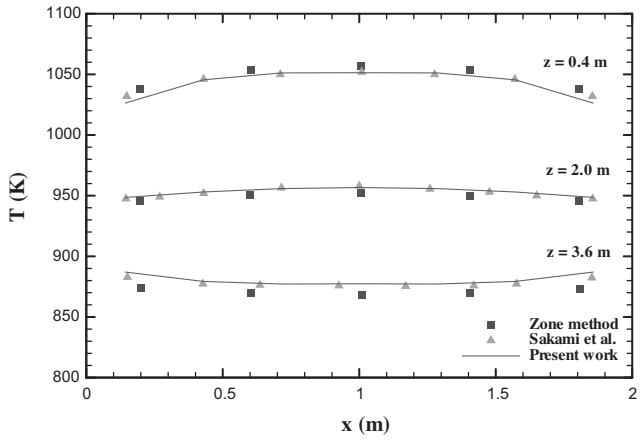

Fig. 4. Temperature distribution of the medium at $y = 1$ m for different values of z; comparison with the results of Sakami et al. and with the zone method ($\omega = 0$, $\kappa = 0.5$ m^{-1} and $\dot{q}''' = 5$ kW/m^3).

4.3. Sensitivity analysis

In order to check the grid independency for convection part of the problem, two cases are considered: 41 × 41 and 81 × 81 convective grid numbers. These grids are refined near the walls in order to avoid excessive temperature steps imposed by the boundary conditions. Several coupled radiation and natural convection problems are solved. Table 2 shows the results for average overall Nusselt number at hot wall obtained for two different Rayleigh numbers ($Ra = 10^5$and 10^6) and three different optical thicknesses ($\tau = 0$, 1 and 5). For radiation part 41 × 41 radiative grid numbers and S_4 angular quadrature is used. It should be mentioned that optical thickness equal to zero is the case of radiatively transparent medium. The results for both grid numbers are close. However, the velocity distribution is more precise for the finer grid. Therefore,

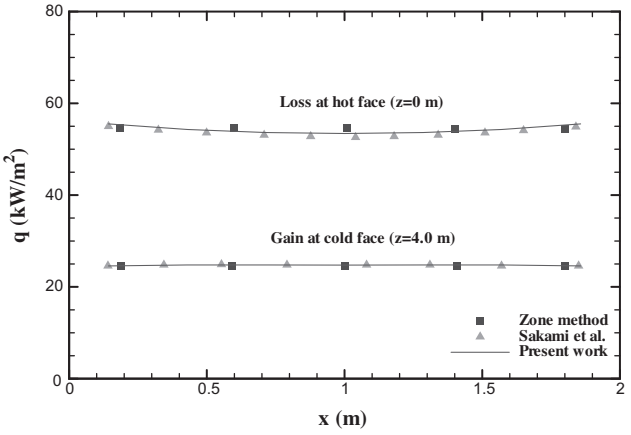

Fig. 5. Radiative net flux distribution of the cold and hot walls for $y = 1$ m; comparison with the results of Sakami et al. and with the zone method ($\omega = 0$, $\kappa = 0.5\ \mathrm{m}^{-1}$ and $\dot{q}''' = 5\ \mathrm{kW/m^3}$).

we used 81×81 convective grid numbers for all the cases presented hereinafter (Fig. 2(b)).

Obtaining the precise results at high optical thicknesses needs another check for radiation part of the problem. Table 3 shows the results of average Nusselt number at $Ra = 10^5$ and 10^6 with three different radiative grid numbers for optical thickness $\tau = 10$. The percentage of differences between each two values has been also displayed.

According to results of Table 3 and the other results in the literature [34,35], the radiative grid numbers is selected to have the average optical thickness of all control volumes less than 0.2. Therefore, in order to have optimum situation between accuracy and computational time, the radiative grid numbers are selected depends on the optical thicknesses shown in Table 4.

In order to have a view of computational time, CPU time for some case problems are shown in Table 5. All computations were carried out for $Ra = 10^6$ and by 1 CPU of an Intel Core 2 Quad operation machine (model name: Q6700, number of CPUs: 4, CPU frequency: 2.66 GHz, memory size: 8 GB) at Tohoku University.

Also, other coupled radiation and natural convection problems are solved to select the appropriate angular quadrature for the DOM.

Table 6 shows the average overall Nusselt number at hot wall obtained with S_4 and S_8 for Rayleigh numbers $Ra = 10^5$ and 10^6 and optical thicknesses $\tau = 1$ and 5. For both angular quadratures, results are close to each other. Thus, in order to reduce the computational effort, we used S_4 angular quadrature for all cases.

5. Results and discussion

In all numerical results presented hereinafter the domain is the one shown in Fig. 1 under normal room conditions. The hot and cold walls are maintained at temperature 310 K and 290 K, respectively. The cavity is filled with a gas of $Pr = 0.717$. Thermophysical properties of the gas are in general considered to be constant and temperature independent and are evaluated at $T_{ave} = 300$ K. All walls are black and the gas is absorbing-emitting medium against thermal radiation. According to the previous results in the literature [19,21,22], the scattering has hardly any effect on the heat transfer in the cavity, therefore it is omitted in this work.

Figs. 6 and 7 show the isotherms and streamlines at $Ra = 10^6$ for 11 different optical thicknesses in a broad range from 0 to 100 and also for the case of pure natural convection. Optical thickness $\tau = 0$ shows the results for the case of radiatively transparent medium. It should be mentioned that if air is considered as fluid in the cavity, the maximum optical thickness for the studied problem becomes about $\tau = 0.1$. However, the purpose of considering high optical thickness in this work is to investigate the behaviors of the cavity with coupled radiation and natural convection at high optical thicknesses.

As seen in Fig. 6, by increasing optical thickness from $\tau = 0$ to $\tau = 2$ the temperature distribution at the core of cavity becomes more homogeneous because of radiation effect. But when optical thickness increases from $\tau = 5$ to $\tau = 100$, absorption of radiation intensities progressively increases and a recursive behavior is observed. Thus, again the isotherms become stratified. Also, it is seen that by growth in optical thickness, the isotherms of pure natural convection case will be obtained. In fact, when optical thickness becomes very large ($\tau > 100$), all of the radiation intensities are absorbed near the walls and cannot penetrate in the cavity. Therefore, the cavity with large optical thickness is like the one without radiation heat transfer (i.e. pure natural convection).

Another important observation in these figures is the behavior of temperature gradients near the horizontal walls. It is seen that

Table 2
Average overall Nusselt number at different optical thickness and convective grid numbers.

$\overline{Nu}_{ove,h}$	$Ra = 10^5$			$Ra = 10^6$		
	$\tau = 0$	$\tau = 1$	$\tau = 5$	$\tau = 0$	$\tau = 1$	$\tau = 5$
41×41	10.128	8.364	6.779	20.644	17.128	14.456
81×81	10.118	8.349	6.776	20.667	17.120	14.462

Table 3
Average overall Nusselt number at different Ra and radiative grid numbers.

$\overline{Nu}_{ove,h}$	25×25	Difference (%)	51×51	Difference (%)	75×75
$Ra = 10^5$	6.314	1.30	6.233	0.37	6.210
$Ra = 10^6$	13.566	0.68	13.474	0.17	13.451

Table 4
Radiative grid numbers for different optical thicknesses.

$\tau < 10$	$\tau = 10$	$\tau = 20$	$\tau > 20$
41×41	51×51	101×101	201×201

Table 5
CPU time of some case problems.

Case problem specifications	CPU time (h)
Pure convection, 41×41 grid numbers	1
Pure convection, 81×81 grid numbers	5.5
$\tau = 1$, 81×81 convective grid numbers, 41×41 radiative grid numbers	39
$\tau = 100$, 81×81 convective grid numbers, 201×201 radiative grid numbers	187

Table 6
Average overall Nusselt number at different optical thickness and quadrature.

$\overline{Nu}_{ove,h}$	$Ra = 10^5$		$Ra = 10^6$	
	$\tau = 1$	$\tau = 5$	$\tau = 1$	$\tau = 5$
S_4	8.364	6.779	17.128	14.456
S_8	8.367	6.811	17.086	14.514

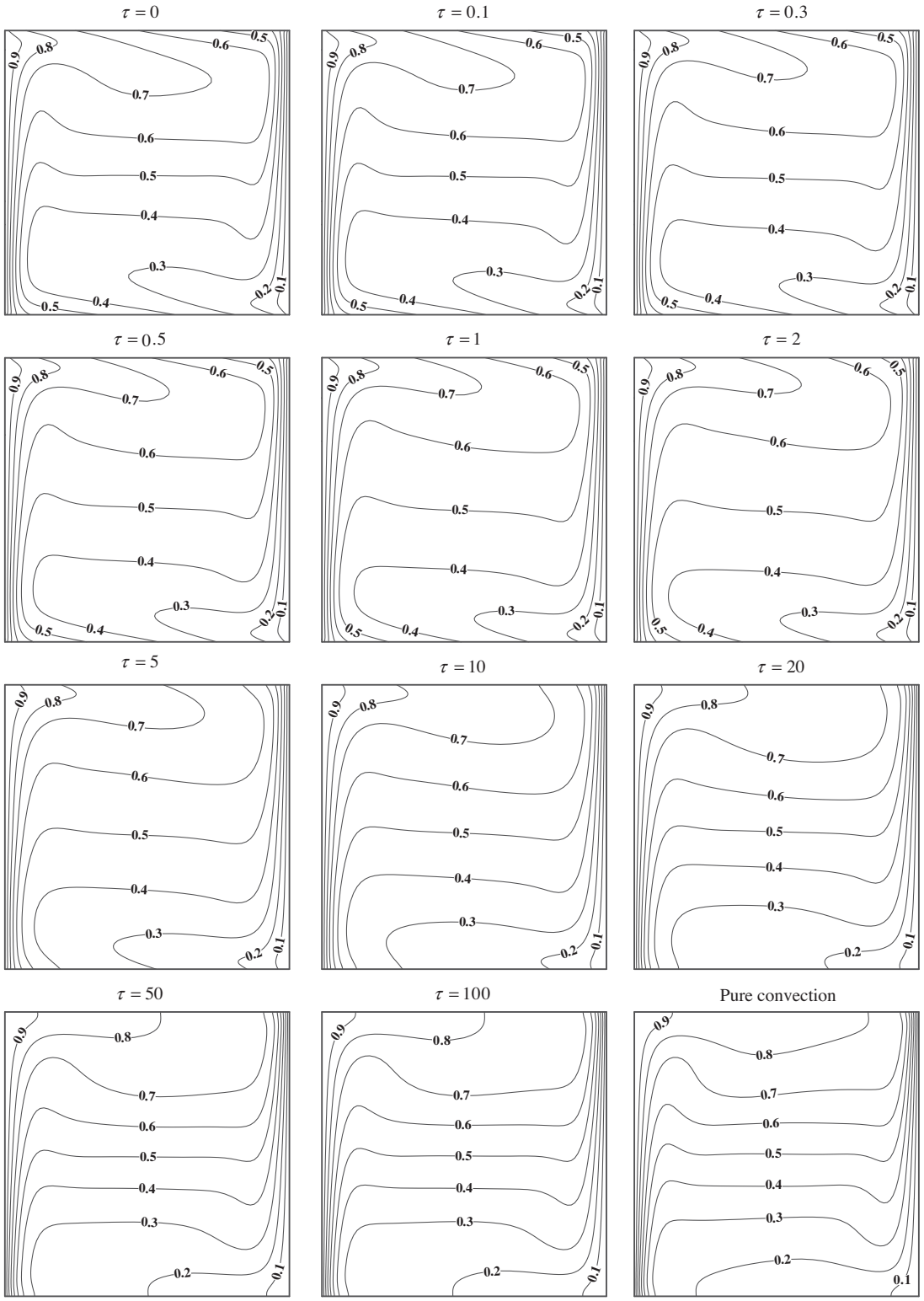

Fig. 6. Isotherms for $Ra = 10^6$ at different optical thicknesses.

temperature gradient gradually decreases with optical thickness. This indicates the importance of the radiative flux at lower optical thicknesses.

Fig. 7 shows the same sweep behavior for streamlines as isotherms. For optical thicknesses from $\tau = 0$ to $\tau = 5$, because of radiation absorbed by gas in the cavity, the stream function gradually increases and fluid rotation and movement fills the most part of the cavity. Therefore in this range, radiation makes the flow field more uniform and the flow rate increases in the cavity. But for optical thicknesses larger than about $\tau = 5$, the radiation is absorbed strongly by the gas near the walls. Hence, conversely, the stream function decreases and streamlines compress near vertical walls to achieve streamlines in pure convection case. This observed behavior confirms that the penetration length of radiation for

about $\tau = 5$ is equal to half of the cavity length, which means up to about $\tau = 5$ all the cavity domain is affected by radiation. Thereafter, increasing the optical thickness decreases the penetration length until reaches to very thin layer near the walls at very high optical thicknesses, which means the affected zone by radiation reduces toward the walls.

The U-velocity distribution along Y-axis (just the top half of it) at $x = L/2$ for different optical thicknesses and three Ra is shown in Fig. 8. The sweep behavior explained previously can be also seen in this figure. For both $Ra = 10^6$ and $Ra = 10^4$ (Fig. 8(a) and (b)), the maximum of U-velocity gradually increases for optical thicknesses from $\tau = 0$ to $\tau = 5$ and after that this maximum decreases with increase in optical thickness until it reaches the pure convection

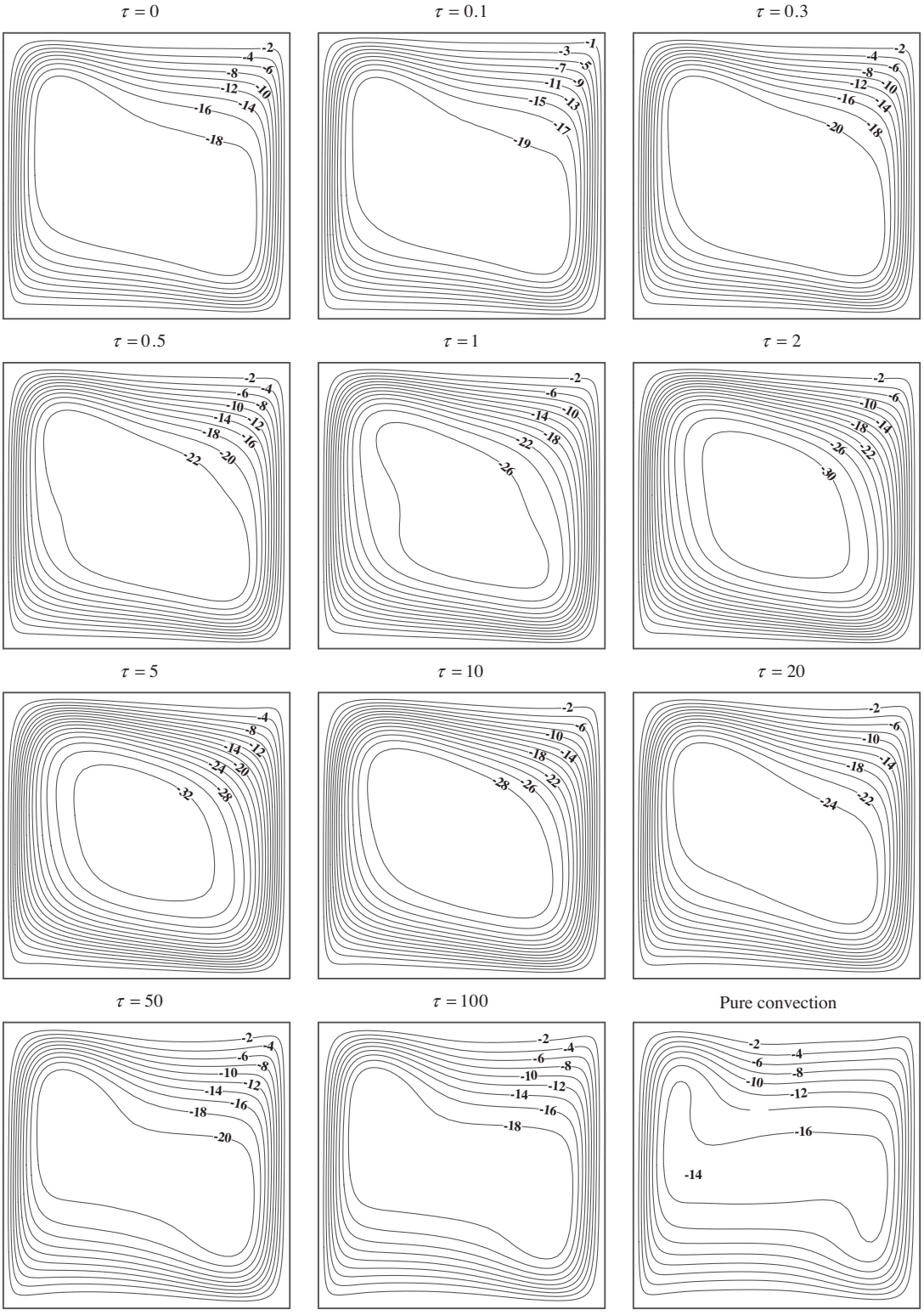

Fig. 7. Streamlines for $Ra = 10^6$ at different optical thicknesses.

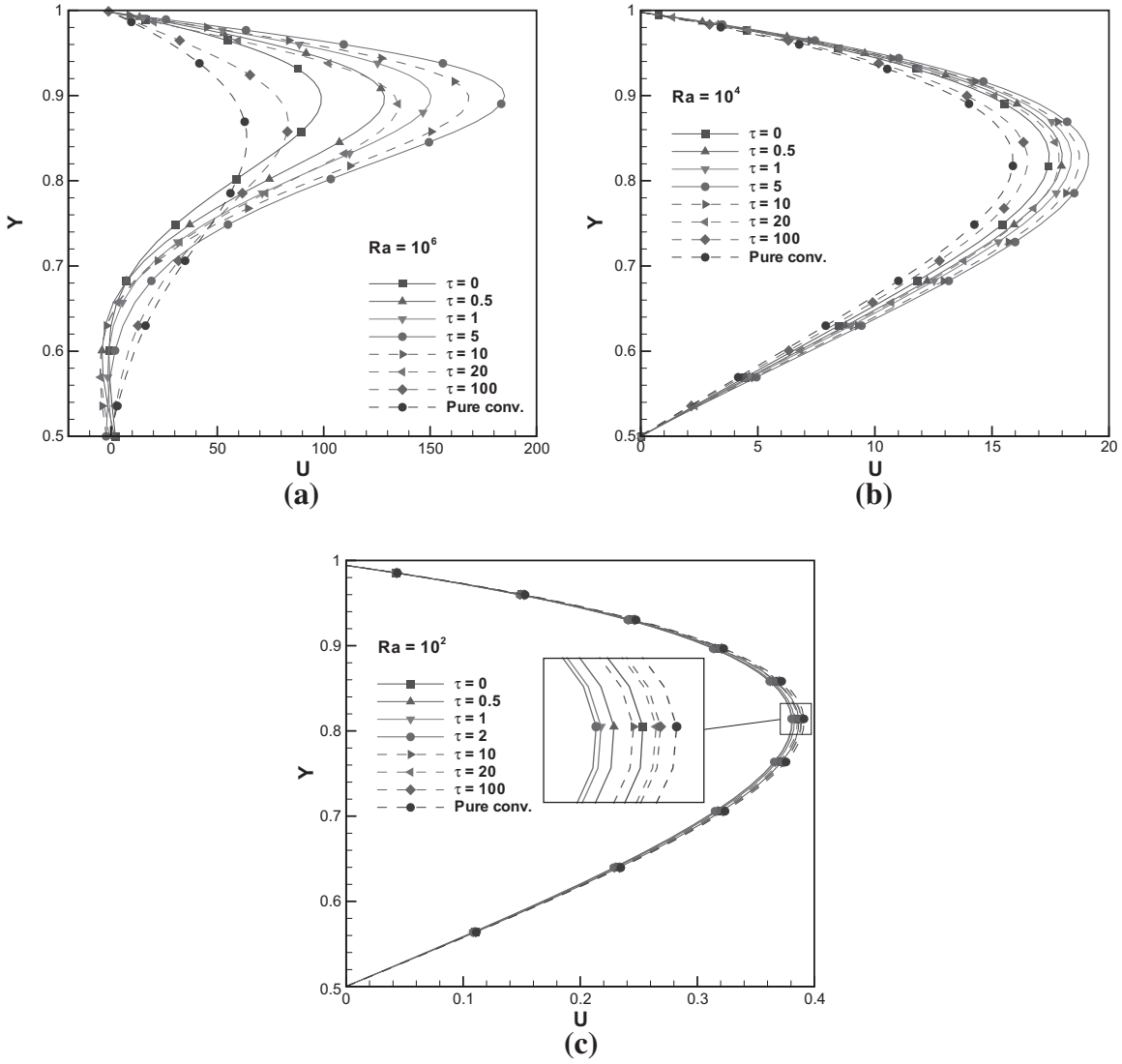

Fig. 8. *U*-velocity along the *Y*-axis at $x = L/2$ for different optical thicknesses and pure convection: (a) $Ra = 10^6$, (b) $Ra = 10^4$, and (c) $Ra = 10^2$.

case. Indeed, due to increasing gas absorption the heat transferring in the cavity increases and hence the driven buoyancy force increases. Thus, higher velocities are acquired. But with more increase in gas absorption, radiation energy cannot penetrate to the core of the cavity and heat transfer decreases. Therefore, velocities decrease.

For $Ra = 10^2$ (Fig. 8(c)) the sweep behavior is observed but in the reverse direction. It means that for optical thicknesses from $\tau = 0$ to $\tau = 2$, the maximum of *U*-velocity gradually decreases and after that with increase in optical thicknesses this maximum increases. This phenomenon is also seen for $Ra = 10^3$ (it has not shown here).

In Fig. 9, the *V*-velocity distribution along *X*-axis (just the right half of it) at $y = L/2$ is seen for different optical thicknesses and three *Ra*. The effects of optical thickness on *V*-velocity are the same as *U*-velocity and they are shown the sweep behavior. Also, from Fig. 9(c), it is seen that like the *U*-velocity, the sweep behavior of *V*-velocity for $Ra = 10^2$ is in the opposite direction relative to the cases with $Ra = 10^4$and 10^6 cases. Therefore, it can be deduced that there are a reverse behavior between the velocity distribution for $10^4 \leqslant Ra \leqslant 10^6$ cases and for $10^2 \leqslant Ra \leqslant 10^3$ cases.

In addition, from both Figs. 8 and 9, it is observed that the amount of velocity and its rate of variation at different optical thicknesses are large at high Rayleigh numbers. This variation for *V*-velocity distribution is smaller than *U*-velocity. On the other hand, the velocity distribution is parabolic at low Rayleigh numbers.

In Fig. 10, the temperature distributions along the *X*-axis at $y = L/2$ are plotted and compared for pure natural convection case and the case with $\tau = 1$ at different *Ra* numbers. For the low Rayleigh numbers ($Ra = 10^2$and 10^3), the temperature distribution is completely linear and it is like the one-dimensional pure conduction heat transfer between two walls at different temperatures. Because, at these Rayleigh numbers the driven buoyancy force is small, thus the flow movement is slow and the natural convection heat transfer is very weak. But with increasing *Ra*, the temperature gradient near the vertical walls increases and a uniform temperature distribution is seen at the core of the cavity. This is because of increase in natural convection which causes the heat transfer at the core part of the cavity to increase. The difference between temperature distribution for $\tau = 1$ and pure convection case at each *Ra*, is very little.

Overall Nusselt number along hot wall is shown in Fig. 11. Fig. 11(a) displays the effect of optical thickness on overall Nusselt number for $Ra = 10^6$. It is seen that the amount of heat flux and therefore Nusselt number is the highest for the radiatively transparent medium ($\tau = 0$) and decreasing progressively for higher optical thicknesses.

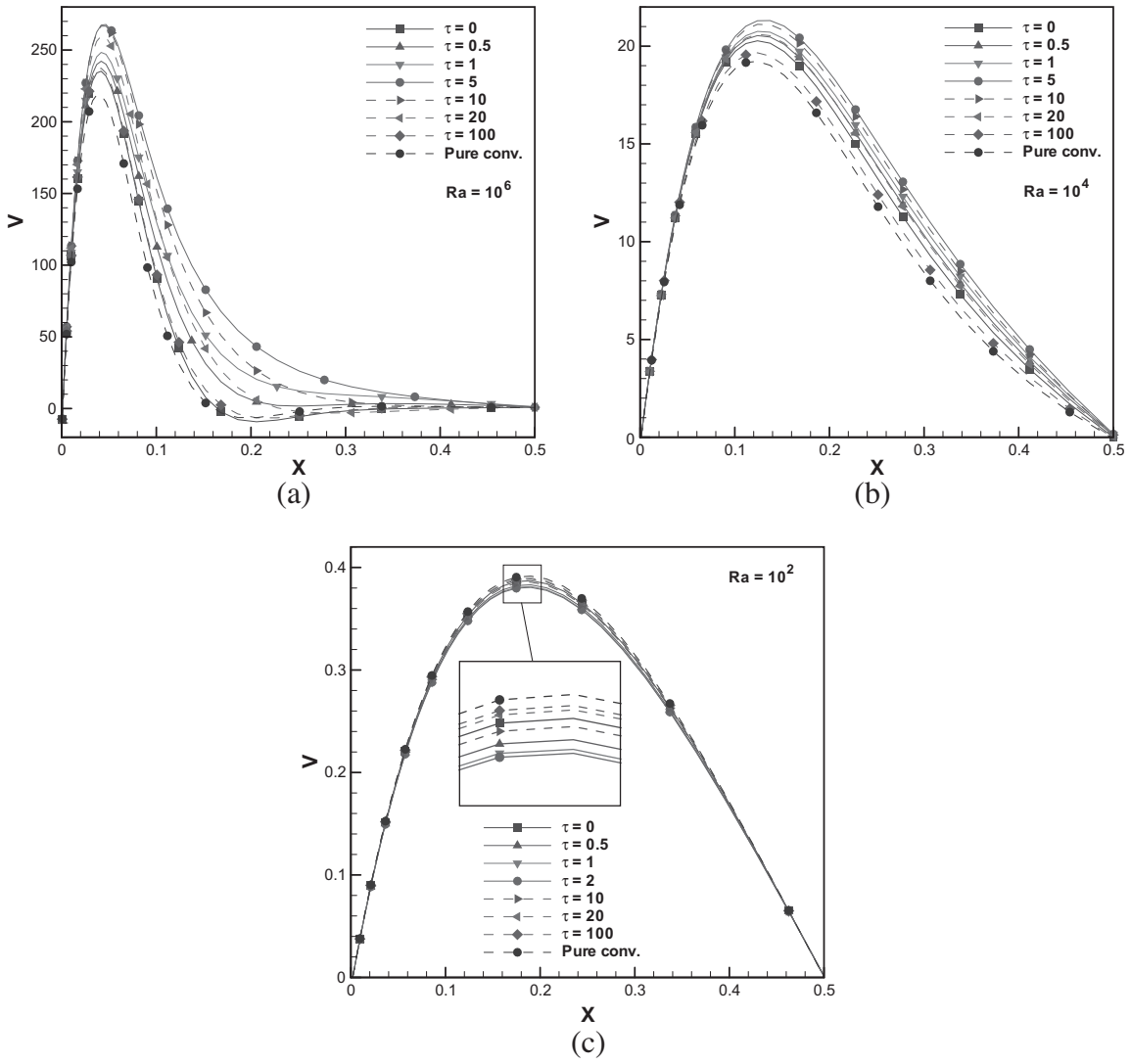

Fig. 9. *V*-velocity along the *X*-axis at $y = L/2$ for different optical thicknesses and pure convection: (a) $Ra = 10^6$, (b) $Ra = 10^4$, and (c) $Ra = 10^2$.

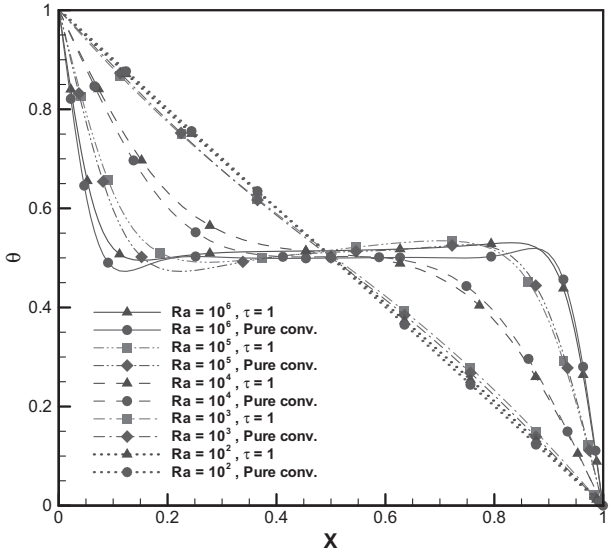

Fig. 10. Temperature along the *X*-axis at $y = L/2$ for different *Ra* at $\tau = 1$ and pure convection.

The pure convection case has smallest Nusselt number and hence, it has minimum amount of thermal exchange with environment. In addition, the difference between overall Nusselt number at bottom and top of the wall increases with increasing the optical thickness. The *Nu* distribution also becomes more uniform for higher optical thicknesses and pure convection.

In Fig. 11(b), the overall Nusselt number at different *Ra* is shown for $\tau = 1$. It is seen that the shapes of Nusselt number distributions are approximately identical for different *Ra,* but the scale of variations is very larger for higher Rayleigh numbers. Because of this scale difference, it is not appropriate to draw all of these curves in one graph. Therefore, they have been drawn in five sticking together graphs.

In Figs. 12 and 13, the average convective, radiative and overall Nusselt numbers and the maximum of stream function at hot wall are plotted for the whole range of optical thickness from 0 to 100 and pure convection case at different *Ra* from 10^2 to 10^6. The horizontal axis of these figures are logarithmic, thus the case of $\tau = 0$, has been shown before $\tau = 0.1$ and has been marked as "Surf. Rad.". Also, the case of pure natural convection has been shown after $\tau = 100$ in these figures and has been specified as "Pure Conv.".

The common phenomenon in all of these figures is that the variation of all of these four parameters is larger for higher Rayleigh

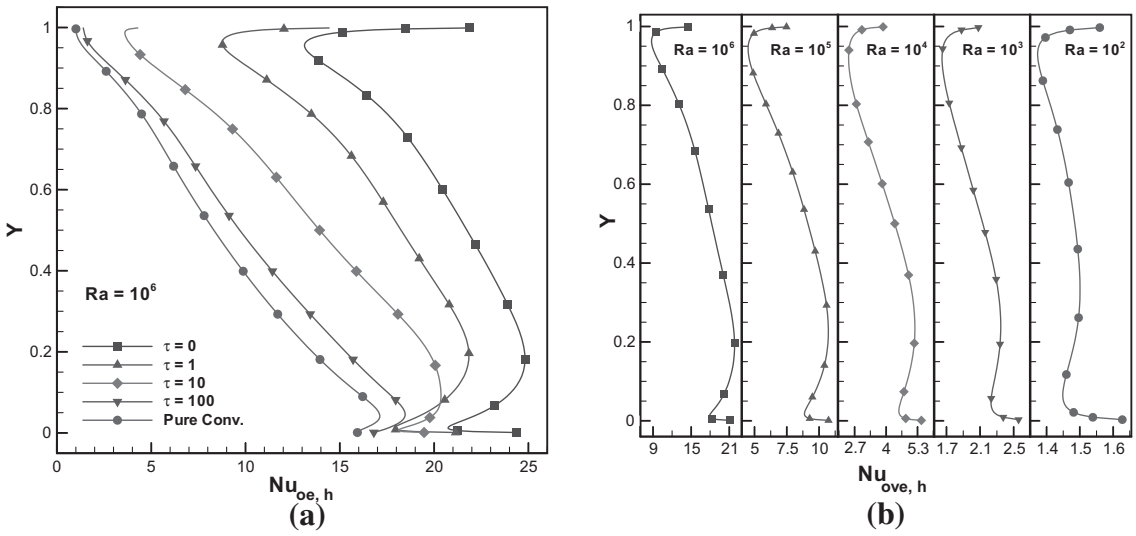

Fig. 11. Overall Nusselt number along hot wall: (a) for $Ra = 10^6$ at different optical thickness and pure convection and (b) for $\tau = 1$ at different *Ra*.

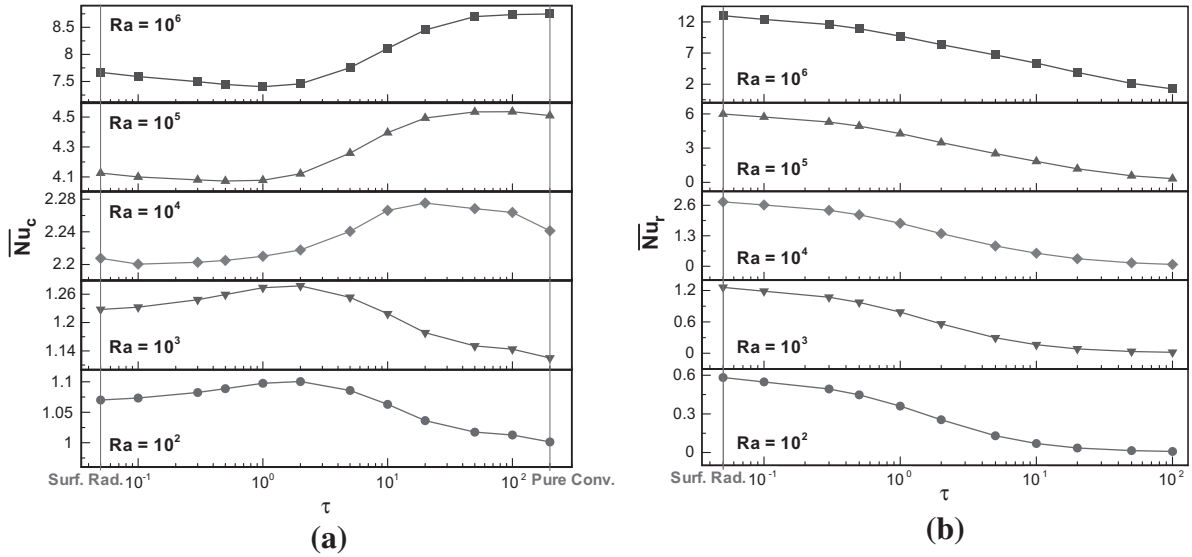

Fig. 12. (a) Average convective Nusselt number at different optical thicknesses for different *Ra* and (b) average radiative Nusselt number at different optical thicknesses for different *Ra*.

numbers. Thus, because of this large difference in the scale of these curves, like the previous figure (Fig. 11(b)), the curves have been drawn in five sticking together graphs.

It is seen from Fig. 12(a) that with neglecting the *Nu* for pure convection, the average convective Nusselt number can be arranged in two categories. The category of high Rayleigh numbers ($10^4 \leqslant Ra \leqslant 10^6$) that have a minimum value in convective Nusselt number distribution along optical thickness, and the category of low Rayleigh numbers ($10^2 \leqslant Ra \leqslant 10^3$) that have a maximum value in this distribution. It should be mentioned that this reverse behavior was seen before in velocity distributions (Figs. 8 and 9).

Fig. 12(b) shows that the average radiative Nusselt number distributions along optical thickness at all Rayleigh numbers have identical behavior. For all cases, the radiative *Nu* decreases with increasing optical thickness. This is because of reduction in radiative heat flux at the hot wall due to increasing the gas absorption. From both Fig. 12(a) and (b) it is seen that at each *Ra*, the variation in radiative *Nu* with optical thickness is larger than that of convective *Nu* number at the same *Ra*. It reveals that the rate of change in radiative heat flux is much larger than that of convective heat flux.

The distribution of average overall Nusselt number along optical thickness in Fig. 13(a) is the same as the radiative *Nu* (Fig. 12(b)). With increasing optical thickness, overall *Nu* decreases until reaches the pure convection *Nu* at very high *Ra*. It is seen that the case of radiatively transparent medium ($\tau = 0$) has the maximum overall *Nu* and hence, it has maximum heat exchange with environment.

The maximum stream function distribution along optical thickness in Fig. 13(b), has the reverse behavior like convective *Nu* (Fig.12(a)). As seen in this figure, like convective *Nu*, the maximum stream function can be settled in two categories. For $10^4 \leqslant Ra \leqslant 10^6$, there is a maximum value in the maximum stream function distribution along optical thickness and inversely, for $10^2 \leqslant Ra \leqslant 10^3$ this distribution has a minimum value. This phenomenon was predictable according to the same behaviors in velocity distribution of the cavity mentioned before (Figs. 8 and

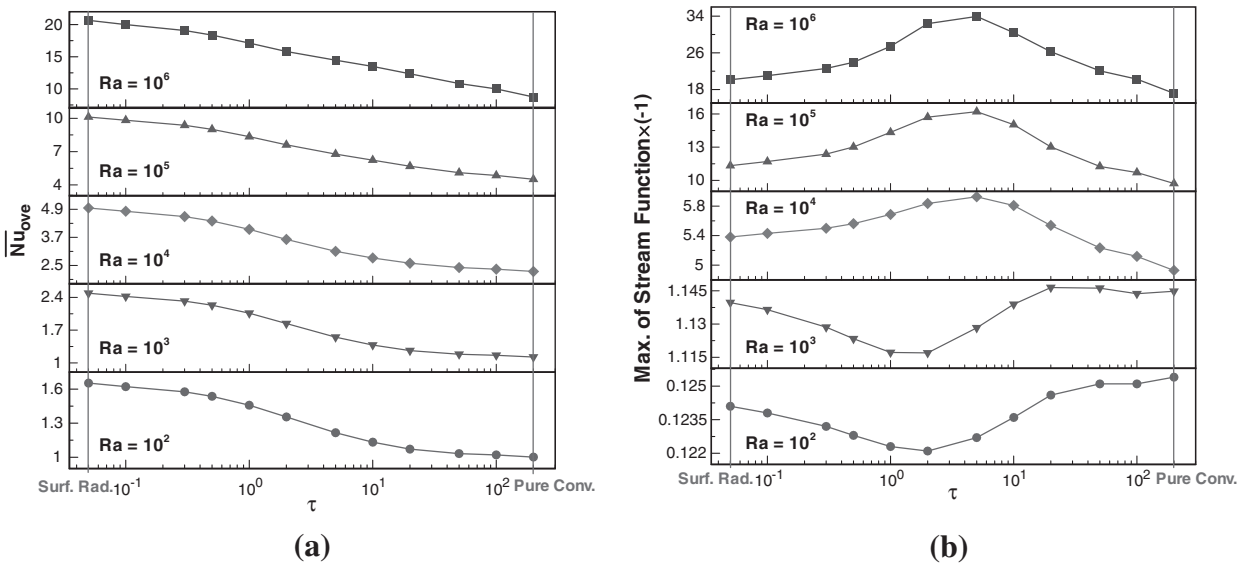

Fig. 13. (a) Average overall Nusselt number at different optical thicknesses for different *Ra* and (b) maximum of streamfunction at different optical thicknesses for different *Ra*.

9). Also, it should be mentioned that despite the variation in the maximum stream function for $10^2 \leqslant Ra \leqslant 10^3$, this variation is very small and the maximum stream function distribution can be considered constant.

6. Conclusions

Combined heat transfer of natural convection and radiation in a 2D square cavity was studied numerically. The continuity, momentum and energy equations were solved by a finite volume method and the radiative transfer equation by discrete ordinates method. The medium was considered emitting-absorbing with black walls. Precise calculation was done to validate the FVM and DOM methods used in this study and also, to check the independency of results from grid numbers and angular quadratures. The heat transfer and flow characteristics of the cavity were analyzed at a broad range of Rayleigh numbers (10^2–10^6) and optical thicknesses (0–100). The following conclusions are obtained from this study:

1. In radiatively transparent medium ($\tau = 0$), radiation is dominant mode of heat transfer, but the contribution of radiation in comparison with convection decrease progressively by increasing optical thickness until the condition of pure convection is obtained.
2. A sweep behavior is observed on the isotherms, streamlines and velocity distributions of the cavity along the optical thickness at each *Ra*. With increase in the optical thickness gradually from zero to a specific value, the variations of each mentioned quantity are in the same direction, but with more increase than the mentioned specific value this direction is inverted.
3. The velocity distributions, maximum stream function and convective Nusselt number have the reverse behavior at different Rayleigh numbers. For $10^4 \leqslant Ra \leqslant 10^6$, maximum velocities and hence maximum stream function distribution along optical thickness have a maximum value. Convective Nusselt number along optical thickness has a minimum value in this range of *Ra*. This behavior is observed inversely for $10^2 \leqslant Ra \leqslant 10^3$.
4. The variation in radiative Nusselt number with optical thickness is several times larger than that of convective Nusselt number at the same *Ra*.
5. The radiative as well as overall Nusselt number on walls decrease with increasing the optical thickness for all Rayleigh numbers. Hence, the radiatively transparent medium ($\tau = 0$) has maximum heat transfer and pure convection case has minimum heat transfer with environment.
6. At very high optical thicknesses, the pure convection condition is again approached for both the thermal features (overall Nusselt number) and the velocity field.

References

[1] G. de Vahl Davis, Natural convection of air in a square cavity: a bench mark numerical solution, Int. J. Numer. Methods Fluids 3 (1983) 227–248.
[2] S.W. Churchill, Free convection in layers and enclosures, in: E.U. Schlünder (Ed.), Heat Exchanger Design Handbook, Hemisphere Publishing, Washington, DC, 1983. pp. 2.5.8.6–2.5.8.13.
[3] N.C. Markatos, K.A. Pericleous, Laminar and turbulent natural convection in an enclosed cavity, Int. J. Heat Mass Transfer 27 (1984) 755–772.
[4] T. Fusegi, J.M. Hyun, K. Kuwaharas, B. Farouk, A numerical study of three-dimensional natural convection in a differentially heated cubical enclosure, Int. J. Heat Mass Transfer 34 (1991) 1543–1557.
[5] G. Barakos, E. Mitsoulis, D. Assimacopoulos, Natural convection flow in a square cavity revisited: laminar and turbulent models with wall functions, Int. J. Numer. Methods Fluids 18 (1994) 695–719.
[6] T. Pesso, S. Piva, Laminar natural convection in a square cavity: low Prandtl numbers and large density differences, Int. J. Heat Mass Transfer 52 (2009) 1036–1043.
[7] M. Jahanshahi, S.F. Hosseinizadeh, M. Alipanah, A. Dehghani, G.R. Vakilinejad, Numerical simulation of free convection based on experimental measured conductivity in a square cavity using water/SiO_2 nanofluid, Int. Commun. Heat Mass Transfer 37 (6) (2010) 687–694.
[8] S. Maruyama, Y. Miyagawa, K. Tsukamoto, T. Aihara, Transient simulation of double diffusive convection of crystal growth in microgravity, in: J.S. Lee, S.H. Chung, K.H. Kim (Ed.), Proceedings of the Sixth International Symposium on Transport Phenomena in Thermal Engineering, Seoul, Korea, May 9–13, 1993, pp. 387–392.
[9] T. Aihara, S. Maruyama, J.S. Choi, Laminar free convection with variable fluid properties in vertical ducts of different cross-sectional shapes, in: C.L. Tien, V.P. Carey, J.K. Ferrell (Ed.), Proceedings of the Eighth International Heat Transfer Conference, San Francisco, CA, 1986, pp. 1581–1586.
[10] S. Maruyama, Laminar free convection in vertical concentric annular ducts, JSME Int. J. Ser. II 31 (2) (1988) 276–282.
[11] X.R. Zhang, S. Maruyama, S. Sakai, Numerical investigation of laminar natural convection on a heated vertical plate subjected to a periodic oscillation, Int. J. Heat Mass Transfer 47 (2004) 4439–4448.
[12] T. Aihara, S. Maruyama, S. Kobayakawa, Free convective/radiative heat transfer from pinfin arrays with a vertical base plate (general representation of heat transfer performance), Int. J. Heat Mass Transfer 33 (6) (1990) 1223–1232.

[13] C. Balaji, S.P. Venkateshan, Interaction of surface radiation with free convection in a square cavity, Int. J. Heat Fluid Flow 14 (3) (1993) 260–267.
[14] K. Velusamy, T. Sundararajan, K.N. Seetharamu, Interaction effects between surface radiation and turbulent natural convection in square and rectangular enclosures, J. Heat Transfer 123 (2001) 1062–1070.
[15] A. Mezrhab, H. Bouali, H. Amaoui, M. Bouzidi, Computation of combined natural-convection and radiation heat-transfer in a cavity having a square body at its center, Appl. Energy 83 (2006) 1004–1023.
[16] M. Behnia, J.A. Reizes, G. de Vahl Davis, Natural convection in a cavity with a window, in: Proceedings of the AIAA 20th Thermophysics Conference, Williamsburg, VA, June 19–21, 1985.
[17] M. Behnia, J.A. Reizes, G. de Vahl Davis, Natural convection in a rectangular slot with convective–radiative boundaries, in: Proceedings of the National Heat Transfer Conference, Denver, CO, 1985.
[18] S. Maruyama, Light Energy Engineering, Yokendo, Tokyo, 2004.
[19] Z. Tan, J.R. Howell, Combined radiation and natural convection in a two-dimensional participating square medium, Int. J. Heat Mass Transfer 34 (3) (1991) 785–793.
[20] C.Y. Han, S.W. Baek, The effects of radiation on natural convection in a rectangular enclosure divided by two partitions, Numer. Heat Transfer Part A 37 (2000) 249–270.
[21] B. Mondal, S.C. Mishra, Simulation of natural convection in the presence of volumetric radiation using the lattice Boltzmann method, Numer. Heat Transfer Part A 55 (2009) 18–41.
[22] P. Kumar, V. Eswaran, A numerical simulation of combined radiation and natural convection in a differential heated cubic cavity, J. Heat Transfer 132 (2010) 023501.1–023501.13.
[23] D.R. Rousse, Numerical predictions of two-dimensional conduction, convection, and radiation heat transfer – I. Formulation, Int. J. Thermal Sci. 39 (2000) 315–331.
[24] S. Chandrasekhar, Radiative Transfer, Clarendon Press, Oxford, 1950.
[25] B.G. Carlson, K.D. Lathrop, Transport thoery – the method of discrete ordinates, in: H. Greenspan, C.N. Kelber, D. Okrent (Eds.), Computing Methods of Reactor Physics, Gordon & Breach, New York, 1968. pp. 165–266.
[26] W.A. Fiveland, Three-dimensional radiative heat transfer solutions by the discrete ordinates method, J. Thermophys. 2 (1988) 309–316.
[27] J.S. Truelove, Three-dimensional radiation in absorbing–emitting–scattering in using the discrete-ordinates approximation, J. Quant. Spectrosc. Radiat. Transfer 39 (1988) 27–31.
[28] S.C. Mishra, H.K. Roy, N. Misra, Discrete ordinate method with a new and a simple quadrature scheme, J. Quant. Spectrosc. Radiat. Transfer 101 (2006) 249–262.
[29] S.V. Patankar, Numerical Heat Transfer and Fluid Flow, Hemisphere Publishing, Washington, DC, 1980.
[30] J.Y. Murthy, S.R. Mathur, Draft Note on Numerical Methods in Heat Mass, and Momentum Transfer, Purdue University, West Lafayette, 2002.
[31] M.F. Modest, Radiative Heat Transfer, second ed., Academic Press, San Diego, 2003.
[32] C.W. Hirt, B.D. Nichols, N.C. Romero, A Numerical Solution Algorithm for Transient Fluid Flows, Los Alamos Scientific Laboratory Report, LA-5852, 1975.
[33] M. Sakami, A. Charette, V.L. Dez, Radiative heat transfer in three-dimensional enclosures of complex geometry by using the discrete-ordinates method, J. Quant. Spectrosc. Radiat. Transfer 59 (1998) 117–136.
[34] S. Maruyama, Radiative heat transfer in anisotropic scattering media with specular boundary subjected to collimated irradiation, Int. J. Heat Mass Transfer 41 (1998) 2847–2856.
[35] S. Maruyama, T. Aihara, Radiation heat transfer of arbitrary three-dimensional absorbing emitting, and scattering media and specular and diffuse surfaces, J. Heat Transfer 119 (1997) 129–136.